

## Article

# The Conjugate of Rhein–Artesunate for Inducing Immunogenic Cell Death to Prepare Cancer Vaccine and Suppress Tumor Growth

Zi-Jian Xu , Wei Wang and Shi-Wen Huang \*

Key Laboratory of Biomedical Polymers of Ministry of Education, Department of Chemistry, Wuhan University, Wuhan 430072, China; 2020202030150@whu.edu.cn (Z.-J.X.); wangweiwhu2020@163.com (W.W.)

\* Correspondence: swhuang@whu.edu.cn

**Abstract:** The conjugate of rhein and artesunate have shown promising effects in inducing immunogenic cell death (ICD) and inhibiting tumor growth. Rhein, a natural anthraquinone derivative found in various medicinal plants such as *Rheum palmatum*, possesses diverse pharmacological properties including anti-inflammatory and anticancer activities. Artesunate, a sesquiterpene lactone extracted from *Artemisia annua*, exhibits potent antimalarial efficacy and has garnered attention for its potential anticancer properties. Through rational drug design, the conjugation of rhein with artesunate has yielded compounds capable of selectively targeting mitochondria of cancer cells, inducing oxidative stress-mediated ICD, and enhancing the immunogenicity of tumor cells. The conjugate leverages the inherent cytotoxicity of artesunate while incorporating the capability to selectively target the mitochondria of rhein, thereby fostering a special approach to immunotherapy for cancer. Upon accumulation in the mitochondria, these compounds induce the generation of reactive oxygen species (ROS), leading to mitochondrial membrane potential ( $\Delta\Psi_m$ ) reduction and endoplasmic reticulum (ER) stress. Notably, the conjugate exhibits far more potent ICD-inducing properties than their parent compounds. In vivo studies have demonstrated that the vaccine, when treated with the conjugate, effectively suppresses tumor growth.

**Keywords:** rhein; artesunate; immunogenic cell death (ICD); tumor growth inhibition; mitochondria targeting; reactive oxygen species (ROS)



**Citation:** Xu, Z.-J.; Wang, W.; Huang, S.-W. The Conjugate of Rhein–Artesunate for Inducing Immunogenic Cell Death to Prepare Cancer Vaccine and Suppress Tumor Growth. *Chemistry* **2024**, *6*, 345–360. <https://doi.org/10.3390/chemistry6030020>

Academic Editor: George Grant

Received: 15 March 2024

Revised: 23 April 2024

Accepted: 23 April 2024

Published: 25 April 2024



**Copyright:** © 2024 by the authors. Licensee MDPI, Basel, Switzerland. This article is an open access article distributed under the terms and conditions of the Creative Commons Attribution (CC BY) license (<https://creativecommons.org/licenses/by/4.0/>).

## 1. Introduction

In cancer immunotherapy, immunogenic cell death (ICD) serves as a pivotal mechanism for eliciting anti-tumor immune responses [1]. ICD is a regulated form of cell death characterized by the emission of damage-associated molecular patterns (DAMPs), including calreticulin (CRT), high mobility group box 1 (HMGB1), and adenosine triphosphate (ATP) [2]. These DAMPs act as danger signals and immune adjuvants, stimulating the activation of innate and adaptive immunity against cancer cells [3,4]. Specifically, the CRT exposure on the cell surface facilitates the phagocytosis of dying cancer cells by dendritic cells (DCs), while ATP functions as a chemoattractant for recruiting DCs to sites of active ICD [5]. Moreover, HMGB1 released from the nucleus enhances the antigen presentation effect of DCs [6,7]. The interaction between DAMPs and the immune system transforms the tumor microenvironment from an immunologically “cold” state to an immunogenic “hot” state, promoting anti-tumor immune responses [8,9]. Given the stressor-dependent nature of ICD induction, various strategies have been employed to design small molecules, metallic compounds, or nano-platforms to induce ICD by eliciting stress in cancer cells [10–12]. Targeting mitochondria to trigger reactive oxygen species (ROS) generation has emerged as a promising approach to induce ICD, highlighting the importance of mitochondrial ROS in amplifying anti-tumor immune responses [13–15]. This mechanistic insight underscores

the therapeutic potential of ICD in cancer immunotherapy and underscores the importance of exploring novel strategies to enhance ICD induction for improved treatment outcomes.

Mitochondria play a crucial role in cellular homeostasis and function as the powerhouse of the cell, involved in metabolism and signal transduction [16,17]. Studies have shown that mitochondria and the endoplasmic reticulum (ER) interact through mitochondria-associated ER membranes (MAMs) to maintain cellular balance [18,19]. Perturbations in the physiological state of one organelle can affect the other, such as calcium ion overload in mitochondria leading to increased reactive oxygen species (ROS) production and subsequent ER stress [20–22]. This suggests a potential mechanism for inducing immunogenic cell death (ICD) by triggering ROS generation in mitochondria. Targeting agents or nano-materials aimed at mitochondria have been reported to enhance ICD effects by precisely controlling mitochondrial ROS production, as demonstrated in previous studies showing that equivalent amounts of ROS generated in mitochondria can induce stronger ICD effects compared to cytoplasmic generation [23,24]. Therefore, endowing agents with mitochondrial targeting capability is crucial for inducing widespread ICD.

Artemisinin-derived compound artesunate (ARS) is recognized by the World Health Organization as a safe and effective antimalarial drug [25,26]. The peroxy group in ARS endows it with both antimalarial and anticancer activities, reacting with ferrous ions or heme to generate highly reactive and toxic carbon-centered free radicals, thereby inducing cellular oxidative stress [27]. Despite its potential, research on ARS-induced immunogenic cell death (ICD) is limited due to its mild ICD effect resulting from non-specific distribution in the cytoplasm [28]. We hypothesize that the lack of mitochondrial targeting restricts the ICD-inducing potential of ARS. As heme is produced in mitochondria, activating ARS, investigations have focused on delivering ARS to mitochondria to induce ICD through mitochondrial ROS generation [29]. Rhein, used as a mitochondrial-targeting ligand, facilitates effective drug delivery due to its highly negative membrane potential. The synthesis of a mitochondria-targeted artesunate derivative (Rhein-EE-ARS or R-A) demonstrated a higher release of ICD-associated DAMPs compared to non-mitochondrial-targeted ARS, owing to its specific mitochondrial targeting and increased ROS generation capability. The optimization of treatment conditions for R-A resulted in an increased expression of surface calreticulin (CRT), crucial for the immune response induced by cancer cell vaccine. Prophylactic tumor vaccination experiments with R-A treatment showed promising results in terms of establishing robust immune responses, forming persistent immune memory, and enhancing the efficacy of cancer immunotherapy. R-A, as an ICD inducer, expands the application of artemisinin analogs in ICD research.

## 2. Materials and Methods

To couple rhein (Rhe) with artesunate (ARS), we devised a two-step esterification process. Initially, rhein and ethylene glycol underwent the first-step esterification reaction, as depicted in Figure S1A [30]. Subsequently, the resulting product (Rhe-EE) underwent a second-step esterification with artesunate, as illustrated in Figure S1B. The structures of the intermediate Rhe-EE and the target product Rhe-EE-ARS (R-A) were confirmed via  $^1\text{H}$  NMR (Figures S2 and S3). And, the final product R-A was further confirmed by infrared spectroscopy and mass spectrometry (Figures S4 and S5).

## 3. Results

### 3.1. Cell Viability Test In Vitro

The results of the MTT assay in Figure 1 demonstrate the cytotoxic effects of R-A on 4T1 cells, with an  $\text{IC}_{50}$  value of 1.88  $\mu\text{M}$ , all of which are lower than those of Rhe ( $\text{IC}_{50}$  value of 46.70  $\mu\text{M}$ ), ARS ( $\text{IC}_{50}$  value of 37.50  $\mu\text{M}$ ), and the mixture of Rhe and ARS (R/A) ( $\text{IC}_{50}$  value of 14.90  $\mu\text{M}$ ). The toxicity of R-A was also compared with that of the standard cytotoxic drug DOX, revealing that R-A was less potent than DOX ( $\text{IC}_{50}$  value of 0.32  $\mu\text{M}$ ), as shown in Figure S6. Compared to ARS, Rhe-conjugated ARS can readily accumulate

within the mitochondria of cancer cells and react with abundant mitochondrial hemoglobin, generating a significant amount of toxic ROS.

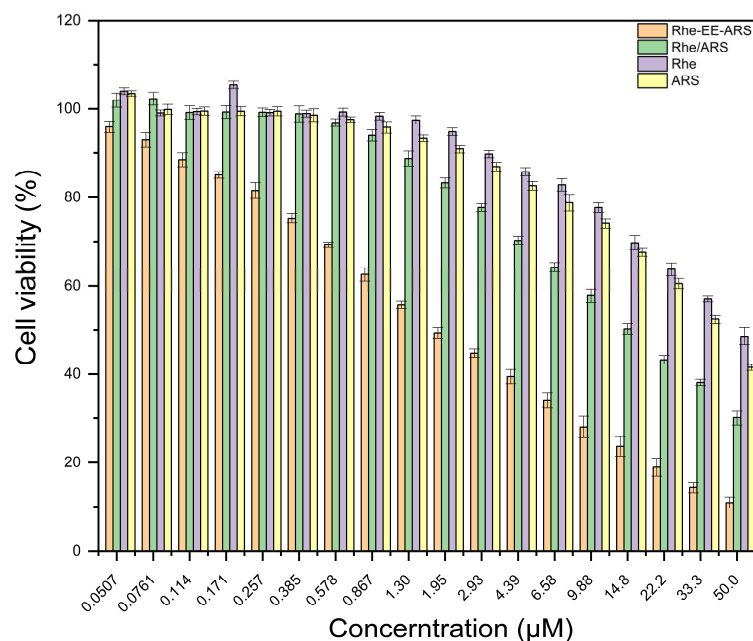


**Figure 1.** In vitro cell viability of 4T1 cells after treatment with Rhe-EE-ARS, Rhe/ARS, Rhe, and ARS.

The quantitative analysis of apoptosis by flow cytometry, as shown in Figure 2, revealed that the total apoptotic rate of 4T1 cells induced by R-A was 57.8%, which significantly higher than that of Rhe (28.4%), ARS (31.2%), and the mixture of Rhe and ARS (R/A) (35.0%). These results are consistent with the findings of the MTT assay. In summary, compared to ARS, the cytotoxicity of R-A is significantly enhanced, attributed to the accumulation of Rhe-ARS conjugate in the mitochondria.

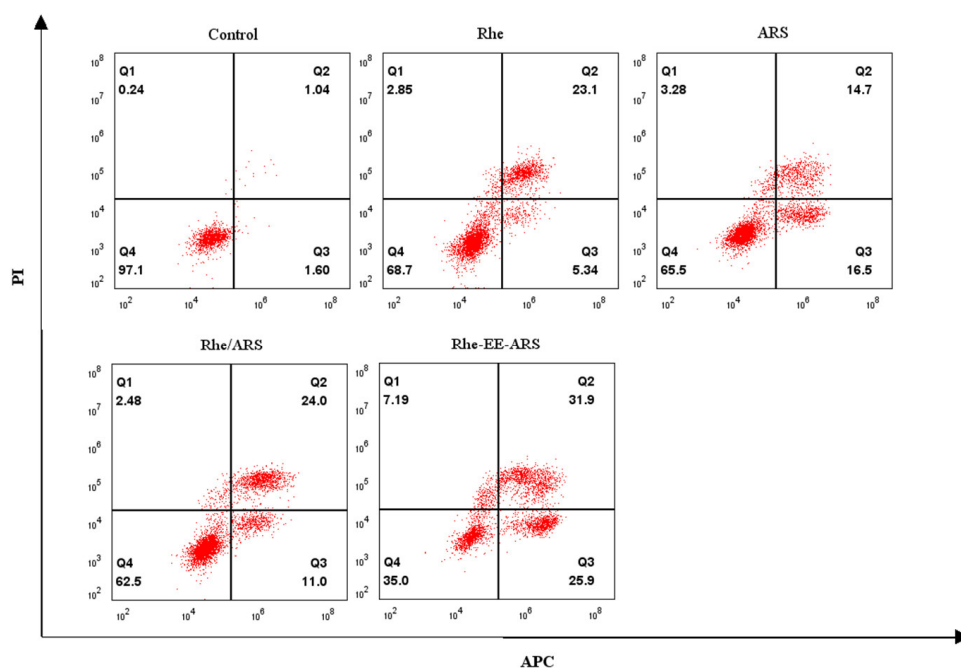


**Figure 2.** Cell apoptosis assay of 4T1 cells after incubation with Rhe-EE-ARS, Rhe/ARS, Rhe, and ARS for 24 h.

### 3.2. Mitochondrial Colocalization

The mitochondria-targeting ability of R-A was assessed. As shown in Figure 3, the green fluorescence of R-A overlaps with the red fluorescence of Mito-Tracker, indicating the mitochondria-targeting capability of R-A. As a control, the mitochondria-targeting ability of Rhe was also evaluated. Pearson correlation coefficients of 0.91 and 0.88 were obtained, indicating that, after 12 h of incubation, R-A mainly localizes within the mitochondria.

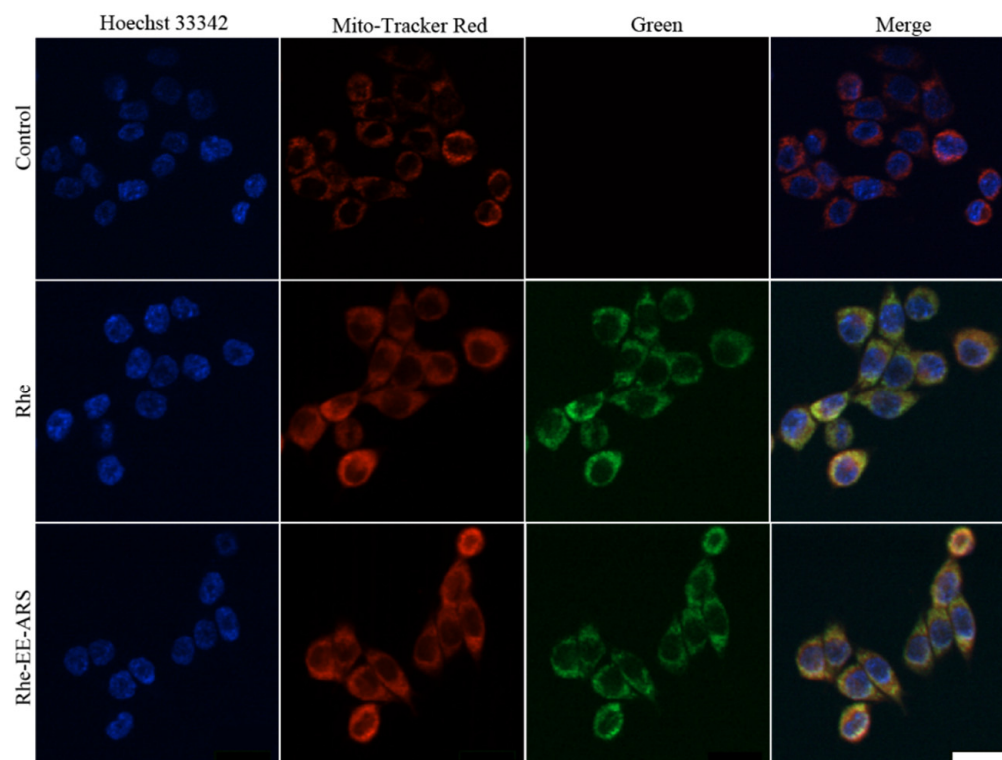


**Figure 3.** CLSM image of 4T1 cells for the co-location of PBS, Rhe-EE-ARS, and Rhe with mitochondria after incubated with PBS, Rhe-EE-ARS, and Rhe for 12 h, scale bar = 20  $\mu\text{m}$ .

### 3.3. Detection of Calreticulin

Under drug-induced cellular stress, calreticulin (CRT), as a hallmark of immunogenic cell death (ICD), is observed to translocate from the endoplasmic reticulum to the membrane of dying cells [31,32]. To investigate whether R-A can induce ICD on a large scale, we quantitatively analyzed the exposure of CRT on the cell surface. We speculate that the CRT expression may be concentration-dependent. After co-incubation with cells at different concentrations (0.25  $\mu\text{M}$ , 0.5  $\mu\text{M}$ , 1  $\mu\text{M}$ , 2  $\mu\text{M}$ , and 4  $\mu\text{M}$ ), CRT expression was measured (Figure 4). After 24 h of co-incubation with R-A, the highest CRT+ expression was observed at a concentration of 2  $\mu\text{M}$ , with the maximum fluorescence intensity (MFI value) reached (Figure S7). Thus, this optimal drug concentration guided subsequent experiments and validated the effectiveness of the previous hypothesis. Additionally, cells treated with R-A exhibited a higher expression of CRT compared to the Rhe, ARS, and R/A groups (Figure 5). Significant differences in CRT expression were observed between cells treated with R-A and those treated with Rhe, ARS, and R/A. This difference demonstrates the important role of R-A in targeting mitochondria to generate excessive ROS and induce CRT expression. CRT expression was also observed by confocal laser scanning microscopy (CLSM) (Figure 6).

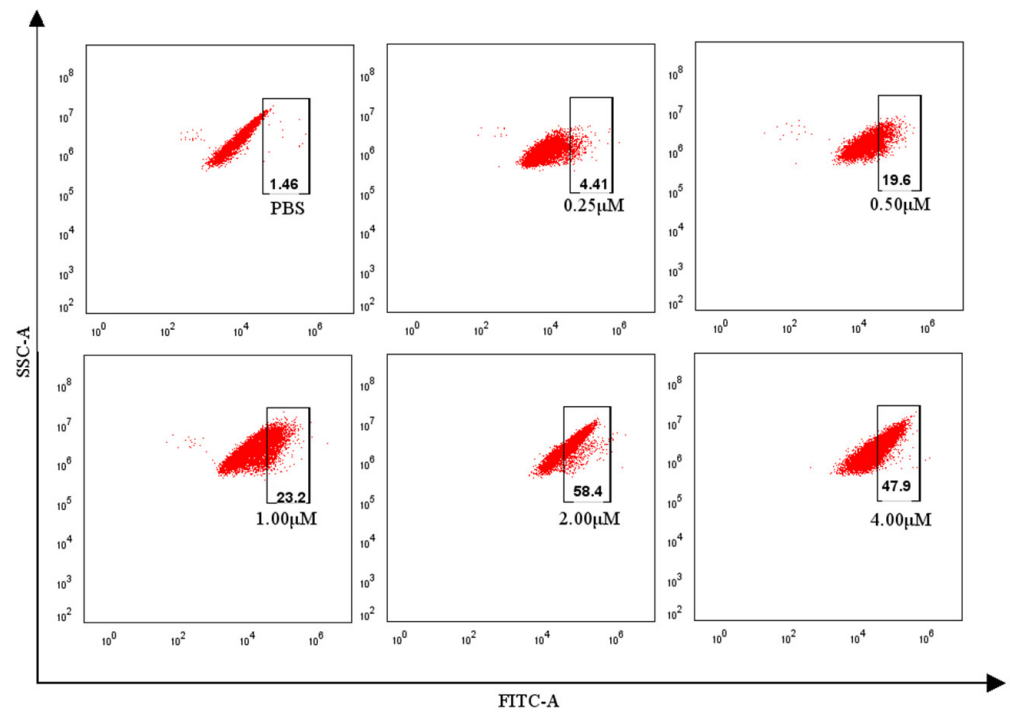


**Figure 4.** Flow cytometry analysis of CRT on the surface of 4T1 cells treated with Rhe-EE-ARS in different concentrations for 24 h.

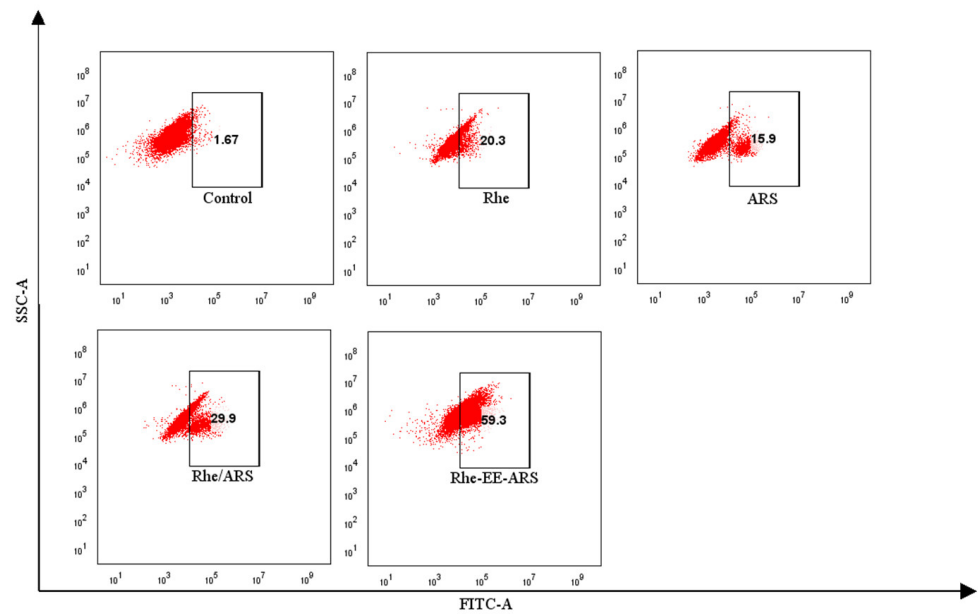


**Figure 5.** Flow cytometry analysis of CRT on the surface of 4T1 cells treated with Rhe-EE-ARS, Rhe/ARS, Rhe, and ARS.

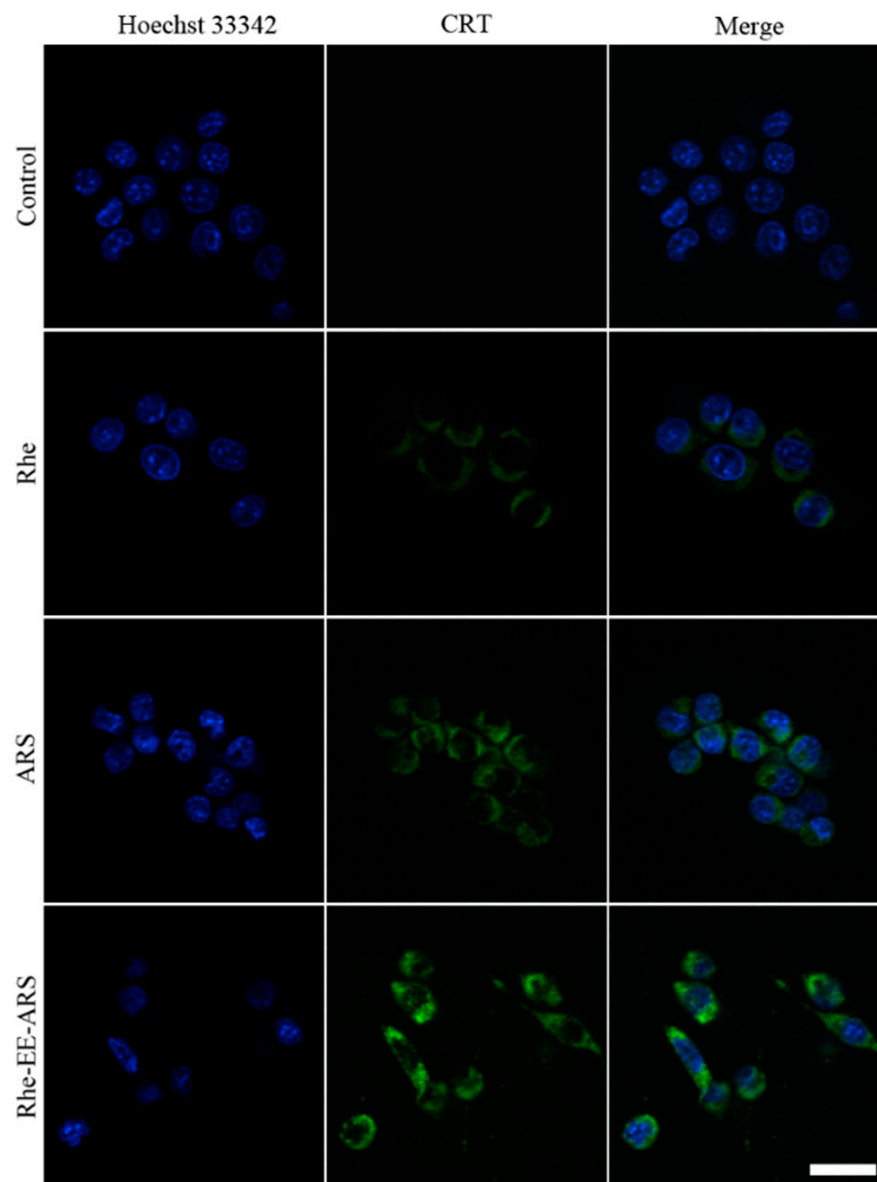


**Figure 6.** CRT translocation onto the cell membrane was observed by CLSM after the 4T1 cells incubation with Rhe-EE-ARS, Rhe, and ARS, scale bar = 20  $\mu\text{m}$ .

### 3.4. Analysis of Reactive Oxygen Species Generation

ROS is crucial for regulating various physiological functions in organisms, while excessive ROS production can disrupt intracellular redox balance, depolarize mitochondrial membranes, elevate caspase levels, and induce apoptosis [33–35]. DCFH-DA and Mito-tracker Red were used as fluorescent probes to monitor ROS generation and cellular localization after treatment with Rhe, ARS, and R-A, respectively. The confocal laser scanning microscopy (CLSM) images in Figure 7 show that treatment with Rhe, ARS, and R-A induces ROS production in 4T1 cells. However, R-A induces more ROS generation than Rhe and ARS within the same treatment time. Furthermore, the level of ROS production was quantified by flow cytometry analysis (Figure 8), showing that cells treated with R-A exhibit a higher ROS generation capacity compared to those treated with Rhe, ARS, and Rhe and ARS mixture (R/A). These results are consistent with the fluorescence imaging results obtained from CLSM.

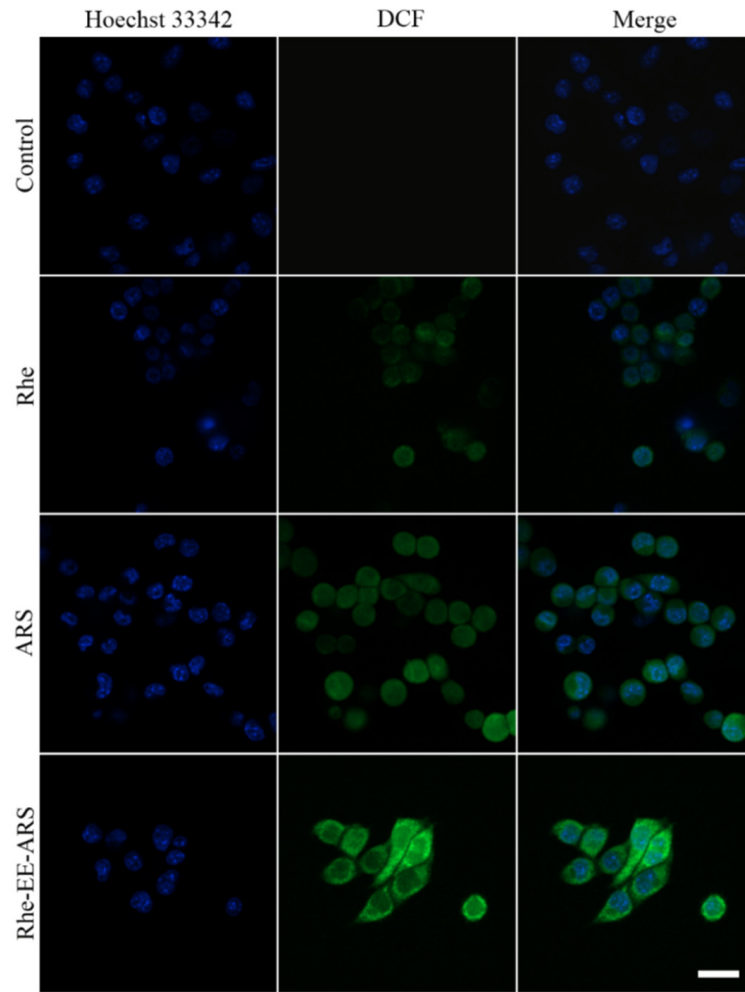


**Figure 7.** CLSM images of 4T1 cells for ROS generation (green fluorescence) after treatment with Rhe-EE-ARS, Rhe, and ARS, scale bar = 20  $\mu\text{m}$ .

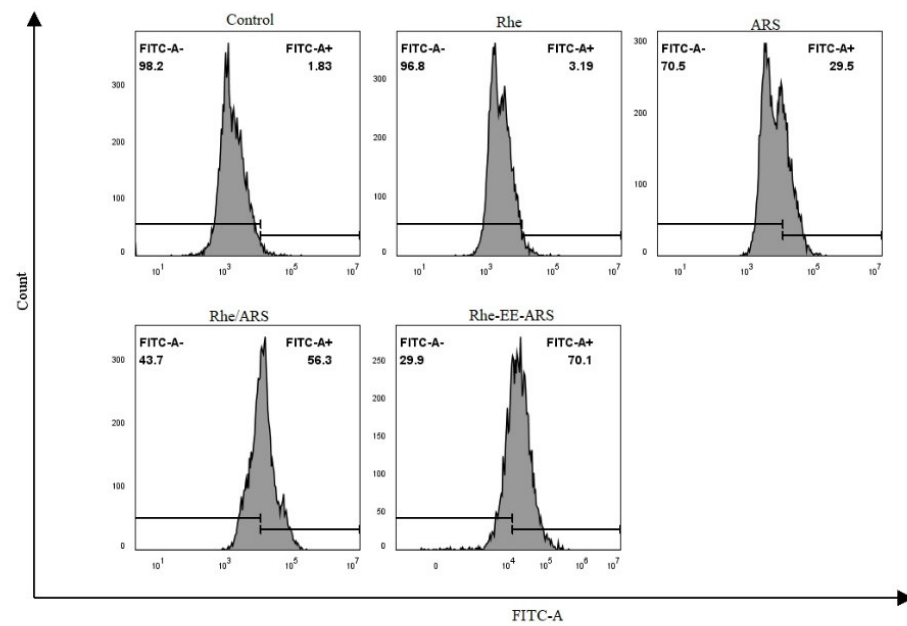


**Figure 8.** Flow cytometry analysis of ROS level in 4T1 cells after treatment with Rhe-EE-ARS, Rhe/ARS, Rhe, and ARS.

### 3.5. Evaluation of Mitochondrial Depolarization

Mitochondrial membrane potential ( $\Delta\Psi_m$ ) is closely related to the physiological status of cells [36,37]. The impact of Rhe, ARS, and R-A on  $\Delta\Psi_m$  was evaluated using JC-1 dye. When JC-1 aggregates in the mitochondrial matrix, it emits red fluorescence, indicating high  $\Delta\Psi_m$ , whereas in damaged mitochondria, it exists in a monomeric form and emits green fluorescence, indicating low  $\Delta\Psi_m$  [38,39]. Cells treated with phosphate-buffered saline (PBS) exhibit strong red fluorescence due to JC-1 aggregation, whereas cells treated with Rhe and ARS show weak red fluorescence, indicating mitochondrial damage. It was observed that cells treated with R-A exhibit the most severe mitochondrial damage, with almost no red fluorescence and the strongest green fluorescence (Figure 9). Flow cytometry analysis yielded similar results (Figure 10), with proportions of green fluorescence after 24 h of treatment with R-A, Rhe, ARS, and R/A being 88.3%, 25.5%, 17.2%, and 41.0%, respectively, indicating that the relative red/green ratio in the R-A group is significantly lower than that in the Rhe, ARS, and R/A groups, leading to more severe mitochondrial damage in cells treated with R-A, providing reliable evidence for the enhancement of  $\Delta\Psi_m$  reduction by R-A via mitochondrial targeting.

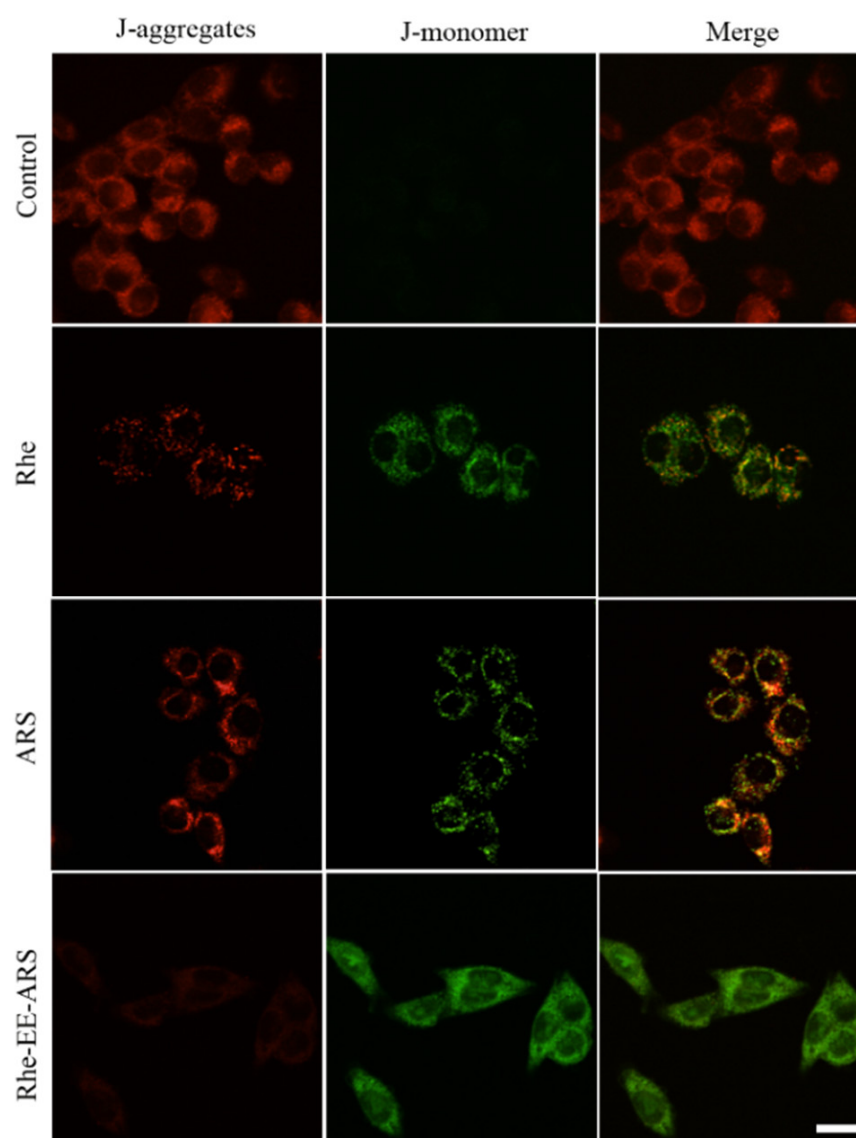


**Figure 9.** CLSM images of 4T1 cells after treated with Rhe-EE-ARS, Rhe, and ARS staining with JC-1, scale bar = 20  $\mu\text{m}$ .

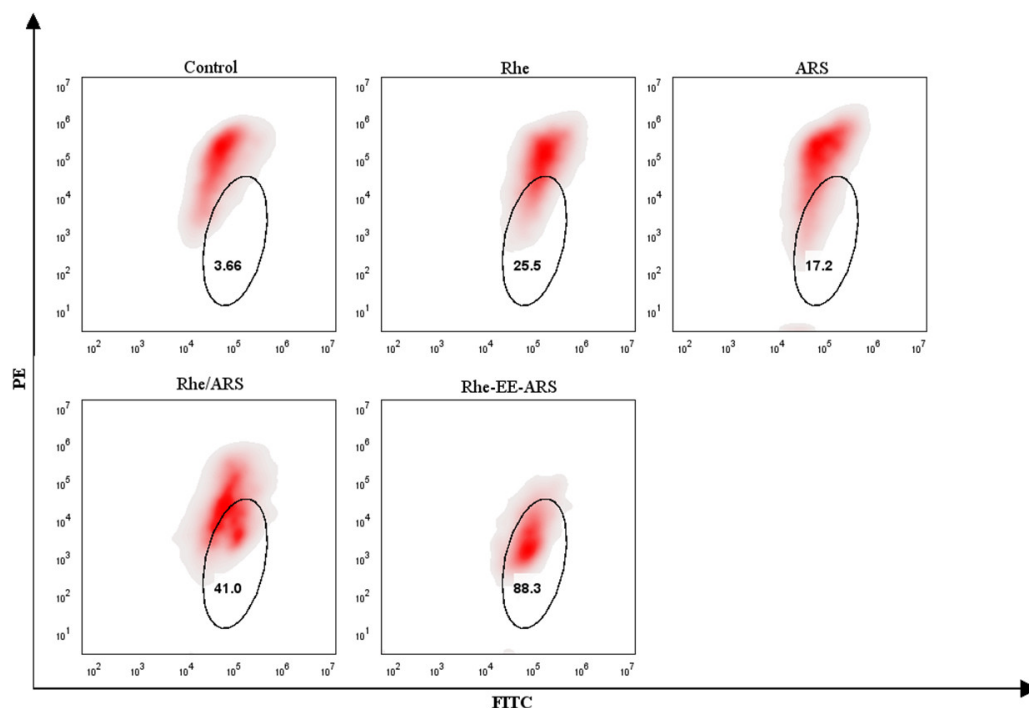


**Figure 10.** 4T1 cells treated with Rhe-EE-ARS, Rhe/ARS, Rhe, and ARS stained with JC-1 were analyzed with flow cytometry.

### 3.6. Detection of ATP and HMGB1

To further confirm the ability of R-A to induce ICD, the release of ATP and HMGB1 from cells was detected. HMGB1 is a typical representative of endogenous danger-associated molecular patterns. Under normal physiological conditions, it functions as an internal DNA-binding protein, stabilizing nucleosomes, and regulating gene transcription [40]. However, when cells undergo external stressors, it is released from the cell nucleus into the extracellular environment. To investigate whether R-A can induce HMGB1 release, as shown in Figure 11, a significant decrease in red fluorescence in both the nucleus and cytoplasm was observed, indicating that a large amount of HMGB1 was released from the cell nucleus into the extracellular environment. In contrast, bright red fluorescence was still observed in the nucleus and cytoplasm of cells treated with Rhe and ARS, predominantly localized in the cell nucleus. The relative average fluorescence intensity values (MFI) of the FITC green fluorescence of HMGB1 were also quantitatively analyzed using Image J (Figure S8), which is consistent with the previously analyzed results.

The amount of extracellular ATP released from cells was also measured. The results show that the amount of ATP secreted in the supernatant of the R-A group is 1.58 times that of the Rhe group, 1.50 times that of the ARS group, and 1.40 times that of the R/A group (Figure 12). These results indicate that, due to its mitochondria-targeting and efficient ROS-generating capabilities, R-A is an excellent ROS-based ICD inducer, offering hope for further exploration into the immunostimulatory ability of R-A-induced ICD-type vaccine.

### 3.7. Tumor Prevention Effect

The X-rays at 60 Gy were used to inactivate the cancer cells for preparing vaccines [41,42]. Vaccines prepared by different treatments are recorded as PBS and R-A groups. The control group received no vaccine. Mice were immunized with the vaccines, administered subcutaneously on the left dorsal side, with two doses administered one week apart. All mice were cared for according to the guidelines for the care and use of laboratory animals, and the procedures were approved by the China Animal Care and Use Committee at Wuhan University.

As shown in the tumor growth curve in Figure 13A, after inoculation with live 4T1 cells, tumors in the control and PBS groups of mice grew rapidly, while tumors in the R-A group grew more slowly. On the 33rd day of the experiment, rapid tumor growth was observed in the control group mice, with an average tumor volume of 1728.8 mm<sup>3</sup>. A weak anti-tumor effect was observed in mice treated with the vaccine that did not induce immunogenic cell death, with an average tumor volume of 1066.1 mm<sup>3</sup> in the PBS group. A significant anti-tumor effect was observed in mice treated with the R-A group vaccine, with an average tumor volume of 627.7 mm<sup>3</sup>. Additionally, two out of five mice in the PBS group and all mice in the R-A group survived for 45 days after receiving live 4T1 cell inoculation, while all mice in the control group died. By day 50, all mice in the PBS group had died, while three out of five mice in the R-A group remained alive. These results confirm that the R-A vaccine, which activates potent in vivo immune responses, significantly delays tumor growth and prolongs the survival of mice (Figure 13B). The tumor inhibition rates for the PBS and R-A groups were 38.3% and 63.7%, respectively. Corresponding tumor weights and photographs were recorded (Figure 13C,D). Compared to the control group, tumors in the PBS group exhibited significantly reduced size and weight, with the R-A group showing the most pronounced inhibition of tumor growth. H&E staining revealed similar results: tumors in the R-A group exhibited larger areas of necrosis, prominent cell separation, and nuclear fragmentation (Figure 13E). These results demonstrate the significant efficacy of the R-A group vaccine in inhibiting tumor growth and metastasis compared to the control group.

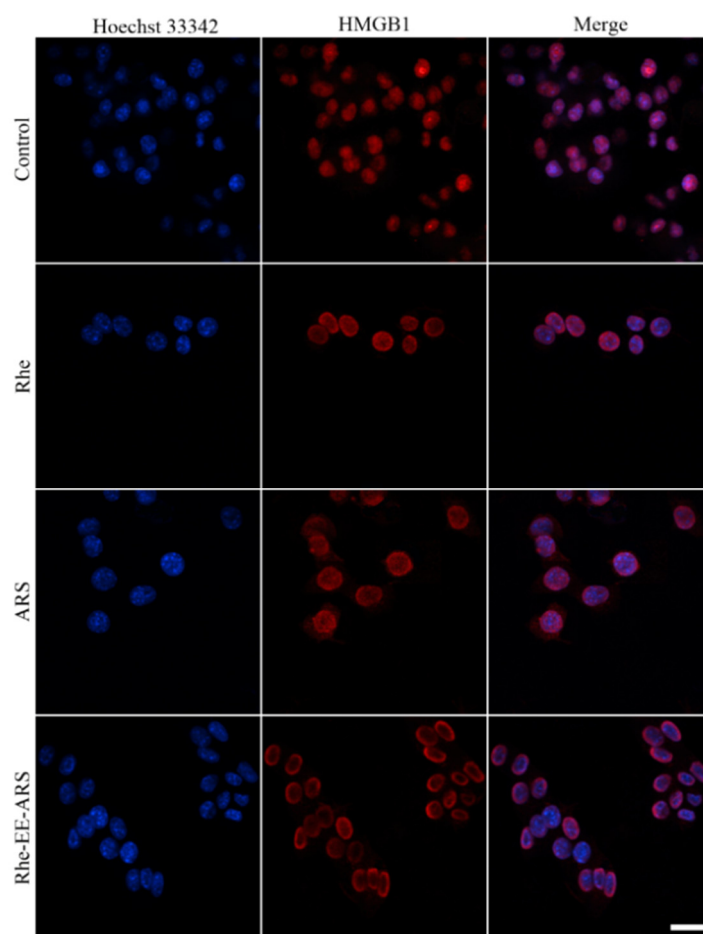


**Figure 11.** CLSM images showing HMGB1 release from the nucleus of 4T1 cells treated with Rhe-EE-ARS, Rhe, and ARS, scale bar = 20  $\mu$ m.

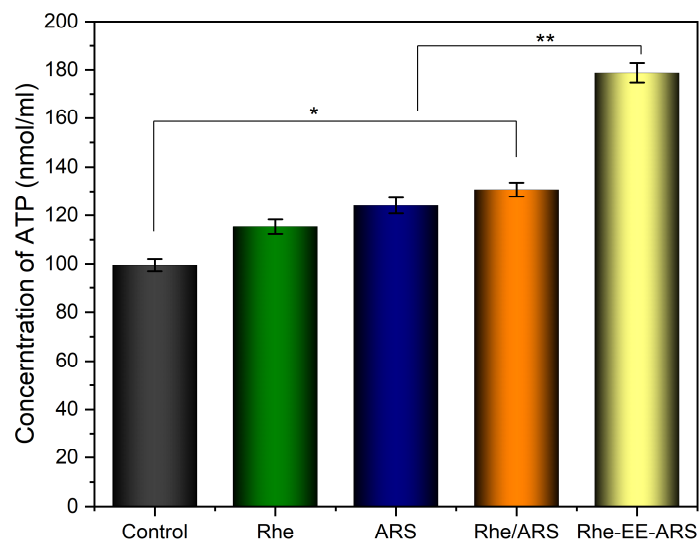


**Figure 12.** The concentration of ATP in 4T1 cells culture medium treated with Rhe-EE-ARS, Rhe/ARS, Rhe, and ARS. Data are presented as mean  $\pm$  S.D. ( $n = 3$ ),  $** p < 0.01$ , and  $* p < 0.05$ .

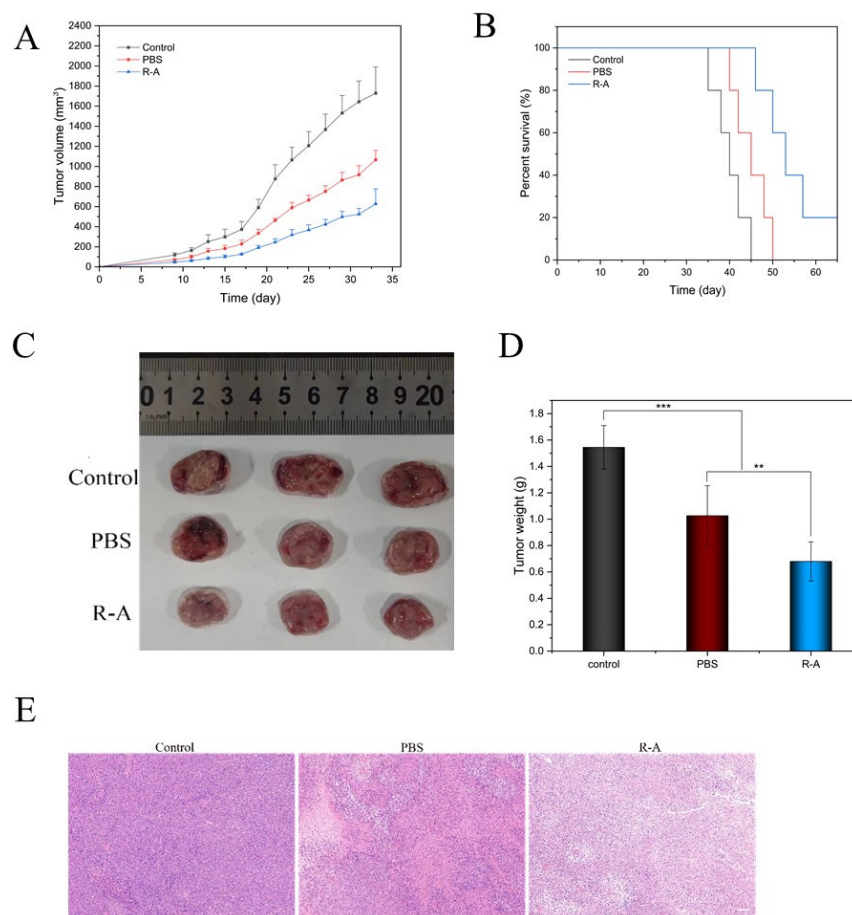


**Figure 13.** (A) Changes in averaged tumor volume after challenge, ( $n = 8$ ). (B) Cumulative survival curves of tumor mice, ( $n = 5$ ). (C) Digital photographs and (D) weight of representative tumors separated from mice after different treatments, ( $n = 3$ ). Data are presented as mean  $\pm$  S.D. ( $n = 3$ ),  $*** p < 0.001$  and  $** p < 0.01$ . (E) H&E staining of the tumor tissues with different treatments, scale bar = 200  $\mu$ m.

### 3.8. Immune Response In Vivo

To validate the anti-tumor immune mechanisms, flow cytometry analysis was performed on immune cells in lymph nodes and tumor tissues after staining with multiple antibodies [43–45]. The results in Figure 14A–D demonstrate that in the R-A group, the percentage of mature DCs (CD80+ CD86+) in lymph nodes increased, while the numbers of effector memory T cells (Tems, CD8+ CD44+ CD62L–) and cytotoxic T lymphocytes (CTLs, CD8+ IFN $\gamma$ +) in tumors increased, accompanied by a decrease in Tregs cells (CD4+ CD25+ Foxp3+). In Figure 14A, the DC cells are gated by CD11c. Cytotoxic T cells in Figure 14B are initially gated by CD3 and then gated by CD8. Similarly, CD4 effector T cells in Figure 14C are first gated by CD3 and then gated by CD4. In Figure 14D, Treg cells are gated first by CD3 and then gated by CD4.

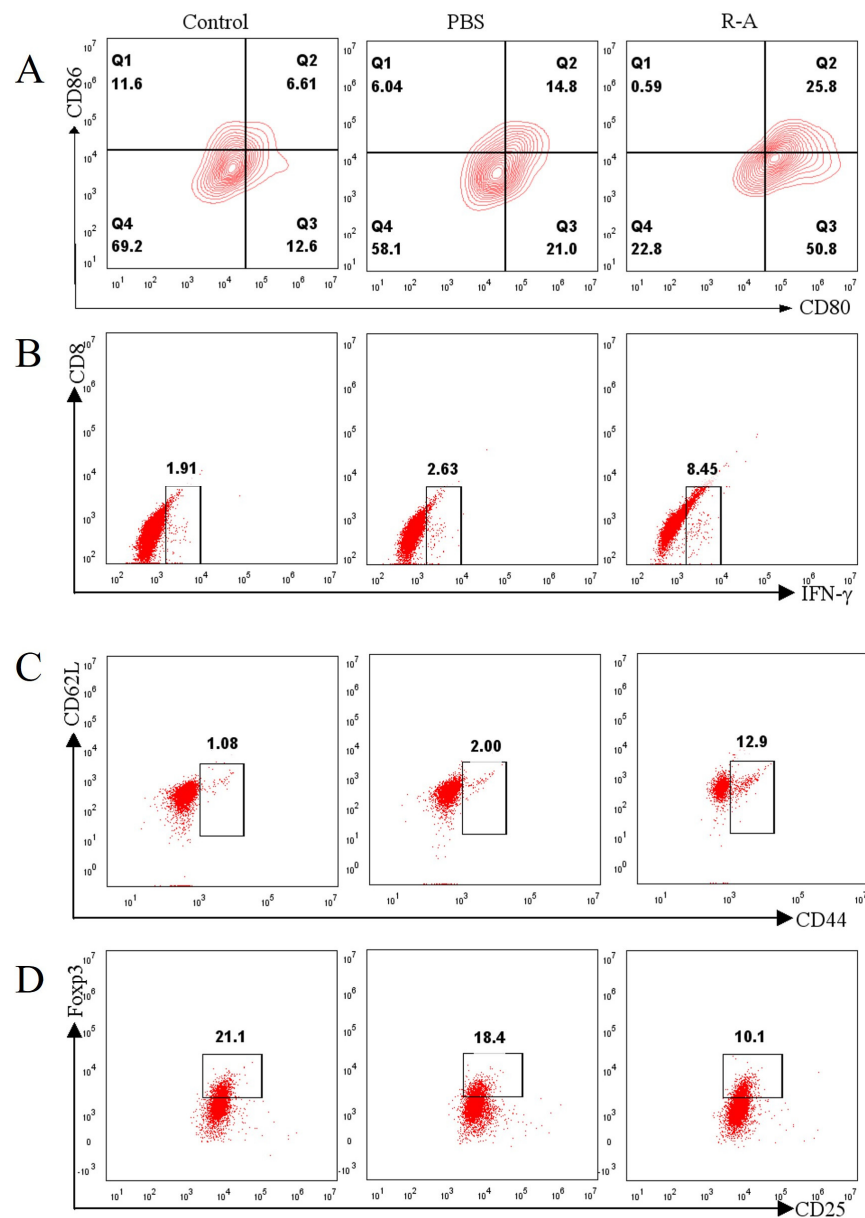


**Figure 14.** (A) Flow cytometric analyses of the populations of DC cells (CD80+ CD86+) in the inguinal lymph nodes of mice immunized by various vaccine formulations. (B) Cytotoxic T cells (CD8+ IFN $\gamma$ ), (C) CD4 effector T cells (CD4+ CD44+ CD62L–), and (D) Treg cells (CD4+ CD25+ Foxp3+) in tumor tissue examined by flow cytometry.

Notably, vaccination with R-A significantly enhanced the maturation of DCs, activating 25.8% of DCs, which is 3.9 times higher than the control group. These results collectively demonstrate the development of a robust anti-tumor immune response within the tumor, attributed to the long-term immune memory effect of the cell vaccine treated with R-A. Naturally, this also suggests that R-A is an excellent ICD inducer, capable of eliciting strong oxidative stress reactions within the mitochondria.

### 3.9. Biosafety of Vaccines

Throughout the entire anti-tumor treatment process, the vaccine's potential side effects on mice were directly assessed by monitoring changes in the body weight of each group, as depicted in Figure S9. No significant changes in body weight were observed in any group of mice. Furthermore, the safety of the vaccines was evaluated. Heart, liver, spleen, kidney, and lung tissues were collected from each group of mice for H&E staining. As shown in Figure S10, histological analysis revealed no observable damage to major organs. Additionally, blood samples were collected from mice in the control, PBS, and R-A groups for hematological analysis, assessing parameters including total white blood cell count (WBC), total red blood cell count (RBC), hemoglobin content (HGB), mean corpuscular volume (MCV), mean corpuscular hemoglobin concentration (MCHC), and platelet (PLT) levels (Figure S11). At the tested doses, the blood components of the mice were within normal ranges. These results demonstrate the vaccine's excellent biosafety profile and suitability for in vivo application.

## 4. Discussion

We successfully synthesized and characterized a novel mitochondria-targeted conjugate of rhein and artesunate, named Rhe-EE-ARS (R-A). Through comprehensive physicochemical analysis and biological experiments, the R-A conjugate was demonstrated as a potent inducer of immunogenic cell death (ICD), suitable for vaccine preparation and tumor prevention. The R-A conjugate induced substantial ICD by generating reactive oxygen species (ROS) within the mitochondria of cells. Subsequently, vaccines were obtained by X-ray inactivation of cells. It was found that the ICD induced by the R-A conjugate cancer cell-killed vaccine effectively activated the immune response, resulting in significant suppression of tumor growth. Overall, R-A conjugate, as an ICD inducer mediated by mitochondrial ROS, provided a promising approach for the application of rhein and artesunate derivatives in the field of ICD. Herein, we delve into the discussion of the study results and outline potential future research directions.

Firstly, through the synthesis and characterization of Rhe-EE-ARS, the successful synthesis of the R-A conjugate was confirmed, and its structure was validated by nuclear magnetic resonance spectroscopy, Fourier-transform infrared spectroscopy, and mass spectrometry. This synthesis method is simple and efficient, providing a reliable synthetic pathway for subsequent studies. Secondly, through cytotoxicity experiments and flow cytometry analysis, it was found that the R-A conjugate exhibited excellent anti-tumor activity and significantly induced the apoptosis of 4T1 breast cancer cells. Compared with the individual use of rhein or artesunate, the R-A conjugate demonstrated stronger cytotoxicity, attributed to its rapid accumulation within the cancer cell mitochondria, leading to the generation of toxic reactive oxygen species (ROS). Additionally, we evaluated the mitochondrial targeting ability of the R-A conjugate. Through confocal laser scanning microscopy and flow cytometry analysis, it was observed that the R-A conjugate efficiently localized within the mitochondria, leading to a significant decrease in mitochondrial membrane potential ( $\Delta\Psi_m$ ) and triggering intracellular oxidative stress response. Further studies revealed that the R-A conjugate effectively induced ICD, activating the immune system through mechanisms such as the increased expression of cell surface calreticulin (CRT), and promoting the release of ATP and HMGB1, thus eliciting a robust in vivo immune response. This provides a theoretical basis for the R-A conjugate as a potential immunogenic vaccine component. Lastly, we validated the anti-tumor activity of the R-A conjugate vaccine in a

mouse model. Through the observation of vaccinated mice and tumor injections, it was found that the R-A conjugate vaccine significantly inhibited tumor growth and metastasis, and prolonged the survival time of the mice. Further analysis of immune cells showed that the R-A conjugate vaccine enhanced the proportion of the mature DCs in lymph nodes, promoted proliferation of effector memory T cells and cytotoxic T lymphocytes, thereby strengthening the anti-tumor immune response in vivo.

Future research could explore the following aspects:

1. Further improvement and optimization of the synthesis method and structure of the R-A conjugate to enhance its synthesis yield and stability. Additionally, the design of more varieties of mitochondria-targeted compounds could be considered to diversify the arsenal of anti-tumor drugs.

2. Delve deeper into the mechanism of ICD induced by the R-A conjugate, including the exploration of signaling pathways related to cell apoptosis, the activation of immune cells, and the impact on the tumor microenvironment, to elucidate the underlying mechanisms of its anti-tumor effects.

3. Conduct more preclinical studies, including in vitro cell experiments and animal model experiments, to verify the safety, effectiveness, and pharmacokinetics of the R-A conjugate-induced ICD cancer cell-killed vaccine. These studies would provide a more comprehensive theoretical and experimental basis for its clinical application.

4. Initiate clinical trials to evaluate the efficacy and safety of the R-A conjugate as an anti-tumor drug or immunogenic vaccine adjuvant, assessing its therapeutic effects and safety in humans, thereby laying the foundation for its ultimate clinical application.

## 5. Conclusions

This study underscores the therapeutic potential of rhein-artesunate conjugate in eliciting immunogenic cell death and suppressing tumor progression, offering insights into the development of innovative cancer therapeutics.

**Supplementary Materials:** The following supporting information can be downloaded at: <https://www.mdpi.com/article/10.3390/chemistry6030020/s1>, Figure S1: Synthesis routes of Rhe-EE (A) and Rhe-EE-ARS (B); Figure S2:  $^1\text{H}$  NMR spectrum (400 MHz) of Rhe-EE in  $\text{CDCl}_3$  at 25 °C; Figure S3:  $^1\text{H}$  NMR spectrum (400 MHz) of Rhe-EE-ARS in  $\text{CDCl}_3$  at 25 °C; Figure S4: The FT-IR of Rhe-EE-ARS; Figure S5: The mass spectrometry of Rhe-EE-ARS; Figure S6: In vitro cell viability of 4T1 cells after treated with Rhe-EE-ARS and free DOX for 48 h; Figure S7: Figure S7 The MFI value of CRT was measured by flow cytometry. Data are presented as mean  $\pm$ S.D. (n = 3), \*\*\*  $p < 0.001$  and \*  $p < 0.05$ ; Figure S8: The MFI value of HMGB1 was measured in CLSM images. Data are presented as mean  $\pm$ S.D. (n = 3), \*\*\*  $p < 0.001$  and \*  $p < 0.05$ ; Figure S9: Body weight changes during different treatments, (n = 8); Figure S10: H&E staining images of heart, liver, spleen, lung and kidney, scale bar = 100  $\mu\text{m}$ ; Figure S11: Blood biochemistry analysis of mice immunized by various vaccine formulations. (A) WBC, RBC, PLT. (B) HGB, MCHC. (C) FL, (n = 3).

**Author Contributions:** Conceptualization, Z.-J.X. and S.-W.H.; methodology, Z.-J.X. and W.W.; validation, Z.-J.X.; data curation, Z.-J.X.; writing—original draft preparation, Z.-J.X.; writing—review and editing, Z.-J.X. and S.-W.H.; project administration, S.-W.H.; funding acquisition, S.-W.H. All authors have read and agreed to the published version of the manuscript.

**Funding:** This research was funded by the National Natural Science Foundation of China, grant number: 52173137 and 51873163.

**Data Availability Statement:** The datasets generated and analyzed during the current study are available from the corresponding author on reasonable request.

**Acknowledgments:** This work was supported by the National Natural Science Foundation of China (52173137, 51873163).

**Conflicts of Interest:** The authors declare no conflicts of interest.

## References

1. Casares, N.; Pequignot, M.O.; Tesniere, A.; Ghiringhelli, F.; Roux, S.; Chaput, N.; Schmitt, E.; Hamai, A.; Hervas-Stubbs, S.; Obeid, M.; et al. Caspase-dependent immunogenicity of doxorubicin-induced tumor cell death. *J. Exp. Med.* **2005**, *202*, 1691–1701. [[CrossRef](#)] [[PubMed](#)]
2. Ding, D.; Jiang, X. Advances in immunogenic cell death for cancer immunotherapy. *Small Methods* **2023**, *7*, 2300354. [[CrossRef](#)] [[PubMed](#)]
3. Garg, A.; Dudek-Peric, A.; Romano, E.; Agostinis, P. Immunogenic cell death. *Int. J. Dev. Biol.* **2015**, *59*, 131–140. [[CrossRef](#)] [[PubMed](#)]
4. Krysko, D.V.; Garg, A.D.; Kaczmarek, A.; Krysko, O.; Agostinis, P.; Vandenabeele, P. Immunogenic cell death and DAMPs in cancer therapy. *Nat. Rev. Cancer* **2012**, *12*, 860–875. [[CrossRef](#)] [[PubMed](#)]
5. Schcolnik-Cabrera, A.; Oldak, B.; Juárez, M.; Cruz-Rivera, M.; Flisser, A.; Mendlovic, F. Calreticulin in phagocytosis and cancer: Opposite roles in immune response outcomes. *Apoptosis* **2019**, *24*, 245–255. [[CrossRef](#)] [[PubMed](#)]
6. Chen, R.C.; Kang, R.; Tang, D.L. The mechanism of HMGB1 secretion and release. *Exp. Mol. Med.* **2022**, *54*, 91–102. [[CrossRef](#)] [[PubMed](#)]
7. Yuan, S.L.; Liu, Z.P.; Xu, Z.R.; Liu, J.; Zhang, J. High mobility group box 1 (HMGB1): A pivotal regulator of hematopoietic malignancies. *J. Hematol. Oncol.* **2020**, *13*, 19. [[CrossRef](#)] [[PubMed](#)]
8. Hernández, Á.P.; Juanes-Velasco, P.; Landeira-Viñuela, A.; Bareke, H.; Montalvillo, E.; Góngora, R.; Fuentes, M. Restoring the immunity in the tumor microenvironment: Insights into immunogenic cell death in onco-therapies. *Cancers* **2021**, *13*, 2821. [[CrossRef](#)] [[PubMed](#)]
9. Zapletal, E.; Vasiljevic, T.; Busson, P.; Glavan, T.M. Dialog beyond the grave: Necrosis in the tumor microenvironment and its contribution to tumor growth. *Int. J. Mol. Sci.* **2023**, *24*, 5278. [[CrossRef](#)]
10. Li, Y.H.; Liu, X.H.; Zhang, X.; Pan, W.; Li, N.; Tang, B. Immunogenic cell death inducers for enhanced cancer immunotherapy. *Chem. Commun.* **2021**, *57*, 12087–12097. [[CrossRef](#)]
11. Zhu, M.Q.; Yang, M.D.; Zhang, J.J.; Yin, Y.Z.; Fan, X.; Zhang, Y.; Qin, S.S.; Zhang, H.; Yu, F. Immunogenic cell death induction by ionizing radiation. *Front. Immunol.* **2021**, *12*, 9. [[CrossRef](#)]
12. Decraene, B.; Yang, Y.H.; De Smet, F.; Garg, A.D.; Agostinis, P.; De Vleeschouwer, S. Immunogenic cell death and its therapeutic or prognostic potential in high-grade glioma. *Genes Immun.* **2022**, *23*, 244. [[CrossRef](#)] [[PubMed](#)]
13. Peng, H.; Yao, F.; Zhao, J.; Zhang, W.; Chen, L.; Wang, X.; Yang, P.; Tang, J.; Chi, Y. Unraveling mitochondria-targeting reactive oxygen species modulation and their implementations in cancer therapy by nanomaterials. *Exploration* **2023**, *3*, 20220115.
14. Li, X.; Fang, P.; Mai, J.; Choi, E.T.; Wang, H.; Yang, X.F. Targeting mitochondrial reactive oxygen species as novel therapy for inflammatory diseases and cancers. *J. Hematol. Oncol.* **2013**, *6*, 19. [[CrossRef](#)] [[PubMed](#)]
15. Yang, Y.; An, Y.H.; Ren, M.L.; Wang, H.J.; Bai, J.; Du, W.L.; Kong, D.Z. The mechanisms of action of mitochondrial targeting agents in cancer: Inhibiting oxidative phosphorylation and inducing apoptosis. *Front. Pharmacol.* **2023**, *14*, 16. [[CrossRef](#)] [[PubMed](#)]
16. Friedrich, V.K.; Rubel, M.A.; Schurr, T.G. Mitochondrial genetic variation in human bioenergetics, adaptation, and adult disease. *Am. J. Hum. Biol.* **2022**, *34*, 25. [[CrossRef](#)]
17. Zhang, X.Y.; Xie, F.; Ma, S.W.; Ma, C.; Jiang, X.; Yi, Y.; Song, Y.F.; Liu, M.Y.; Zhao, P.X.; Ma, X.M. Mitochondria: One of the vital hubs for molecular hydrogen's biological functions. *Front. Cell Dev. Biol.* **2023**, *11*, 15. [[CrossRef](#)]
18. Zhang, Y.; Yao, J.Y.; Zhang, M.M.; Wang, Y.S.; Shi, X.J. Mitochondria-associated endoplasmic reticulum membranes (MAMs): Possible therapeutic targets in heart failure. *Front. Cardiovasc. Med.* **2023**, *10*, 7. [[CrossRef](#)]
19. Yang, M.; Li, C.R.; Yang, S.K.; Xiao, Y.; Xiong, X.F.; Chen, W.; Zhao, H.; Zhang, Q.; Han, Y.C.; Sun, L. Mitochondria-associated membranes—The origin site of autophagy. *Front. Cell Dev. Biol.* **2020**, *8*, 11. [[CrossRef](#)]
20. Chang, A.Y.; Marshall, W.F. Organelles—Understanding noise and heterogeneity in cell biology at an intermediate scale. *J. Cell Sci.* **2017**, *130*, 819–826. [[CrossRef](#)]
21. Woldemichael, T.; Rosania, G.R. The physiological determinants of drug induced lysosomal stress resistance. *PLoS ONE* **2017**, *12*, 22. [[CrossRef](#)]
22. Vaidziulyte, K.; Coppey, M.; Schauer, K. Intracellular organization in cell polarity—Placing organelles into the polarity loop. *J. Cell Sci.* **2019**, *132*, 9. [[CrossRef](#)] [[PubMed](#)]
23. Yang, T.; Zhang, X.F.; Yang, X.; Li, Y.; Xiang, J.J.; Xiang, C.B.; Liu, Z.K.; Hai, L.; Huang, S.P.; Zhou, L.H.; et al. A mitochondria-targeting self-assembled carrier-free lonidamine nanodrug for redox-activated drug release to enhance cancer chemotherapy. *J. Mater. Chem. B* **2023**, *11*, 3951–3957. [[CrossRef](#)]
24. Zeng, Z.; Fang, C.; Zhang, Y.; Chen, C.X.; Zhang, Y.F.; Zhang, K. Mitochondria-targeted nanocarriers promote highly efficient cancer therapy: A review. *Front. Bioeng. Biotechnol.* **2021**, *9*, 12. [[CrossRef](#)]
25. Tu, Y.Y. Artemisinin-A gift from traditional Chinese medicine to the world (Nobel lecture). *Angew. Chem. Int. Ed.* **2016**, *55*, 10210–10226. [[CrossRef](#)] [[PubMed](#)]
26. Adebayo, J.O.; Tijjani, H.; Adegunloye, A.P.; Ishola, A.A.; Balogun, E.A.; Malomo, S.O. Enhancing the antimalarial activity of artesunate. *Parasitol. Res.* **2020**, *119*, 2749–2764. [[CrossRef](#)]
27. Khanal, P. Antimalarial and anticancer properties of artesunate and other artemisinins: Current development. *Mon. Chem.* **2021**, *152*, 387–400. [[CrossRef](#)]
28. Xie, D.Q.; Wang, Q.F.; Wu, G.Z. Research progress in inducing immunogenic cell death of tumor cells. *Front. Immunol.* **2022**, *13*, 27. [[CrossRef](#)]
29. Catanzaro, E.; Feron, O.; Skirtach, A.G.; Krysko, D.V. Immunogenic cell death and role of nanomaterials serving as therapeutic vaccine for personalized cancer immunotherapy. *Front. Immunol.* **2022**, *13*, 18. [[CrossRef](#)] [[PubMed](#)]

30. Cai, J.; Duan, Y.B.; Yu, J.; Chen, J.Q.; Chao, M.; Ji, M. Bone-targeting glycol and NSAIDS ester prodrugs of rhein: Synthesis, hydroxyapatite affinity, stability, anti-inflammatory, ulcerogenicity index and pharmacokinetics studies. *Eur. J. Med. Chem.* **2012**, *55*, 409–419. [[CrossRef](#)]
31. Kim, D.Y.; Pyo, A.; Yun, M.; Thangam, R.; You, S.H.; Zhang, Y.; Jung, Y.R.; Nguyen, D.H.; Venu, A.; Kim, H.S.; et al. Imaging calreticulin for early detection of immunogenic cell death during anticancer treatment. *J. Nucl. Med.* **2021**, *62*, 37. [[CrossRef](#)]
32. Liu, C.; Leclair, P.; Pedari, F.; Monajemi, M.; Sly, L.; Reid, G.R.; Lim, C. Integrin activity reduces immunogenic cell death by inhibiting cell surface presentation of ERp57 and calreticulin. *Mol. Biol. Cell* **2018**, *29*, 1. [[CrossRef](#)]
33. Sharifi-Rad, M.; Kumar, N.V.A.; Zucca, P.; Varoni, E.M.; Dini, L.; Panzarini, E.; Rajkovic, J.; Fokou, P.V.T.; Azzini, E.; Peluso, I.; et al. Lifestyle, oxidative stress, and antioxidants: Back and forth in the pathophysiology of chronic diseases. *Front. Physiol.* **2020**, *11*, 21. [[CrossRef](#)] [[PubMed](#)]
34. Wang, F.; Wang, X.; Liu, Y.P.; Zhang, Z.H. Effects of exercise-induced ROS on the pathophysiological functions of skeletal muscle. *Oxidative Med. Cell Longev.* **2021**, *2021*, 5. [[CrossRef](#)]
35. Sinenko, S.A.; Starkova, T.Y.; Kuzmin, A.A.; Tomilin, A.N. Physiological signaling functions of reactive oxygen species in stem cells: From flies to man. *Front. Cell Dev. Biol.* **2021**, *9*, 21. [[CrossRef](#)] [[PubMed](#)]
36. Zhang, B.; Wang, D.; Guo, F.; Xuan, C. Mitochondrial membrane potential and reactive oxygen species in cancer stem cells. *Familial Cancer* **2015**, *14*, 19–23. [[CrossRef](#)] [[PubMed](#)]
37. Joshi, D.C.; Bakowska, J.C. Determination of mitochondrial membrane potential and reactive oxygen species in live rat cortical neurons. *J. Vis. Exp.* **2011**, *51*, 2704.
38. Sivandzade, F.; Bhalerao, A.; Cucullo, L. Analysis of the mitochondrial membrane potential using the cationic JC-1 dye as a sensitive fluorescent probe. *Bio-Protocol* **2019**, *9*, 13. [[CrossRef](#)] [[PubMed](#)]
39. Mathur, A.; Hong, Y.; Kemp, B.K.; Barrientos, A.A.; Erusalimsky, J.D. Evaluation of fluorescent dyes for the detection of mitochondrial membrane potential changes in cultured cardiomyocytes. *Cardiovasc. Res.* **2000**, *46*, 126–138. [[CrossRef](#)] [[PubMed](#)]
40. Klune, J.R.; Dhupar, R.; Cardinal, J.; Billiar, T.R.; Tsung, A. HMGB1: Endogenous danger signaling. *Mol. Med.* **2008**, *14*, 476–484. [[CrossRef](#)]
41. Bhatia, S.S.; Pillai, S.D. Ionizing radiation technologies for vaccine development—A mini review. *Front. Immunol.* **2022**, *13*, 9. [[CrossRef](#)]
42. Wijewardana, V.; Ulbert, S.; Cattoli, G. Editorial: Irradiation technologies for vaccine development. *Front. Immunol.* **2022**, *13*, 1075335. [[CrossRef](#)] [[PubMed](#)]
43. Yu, Y.R.A.; O’Koren, E.G.; Hotten, D.F.; Kan, M.J.; Kopin, D.; Nelson, E.R.; Que, L.; Gunn, M.D. A protocol for the comprehensive flow cytometric analysis of immune cells in normal and inflamed murine non-lymphoid tissues. *PLoS ONE* **2016**, *11*, 23. [[CrossRef](#)] [[PubMed](#)]
44. Blanchard, L.; Vina, E.; Asrir, A.; Tardiveau, C.; Coudert, J.; Laffont, R.; Tarroux, D.; Bettini, S.; Veerman, K.; Lafouresse, F.; et al. Flow cytometry analysis of endothelial cells and subsets of exhausted CD8+ T cells in murine tumor models. *Star Protoc.* **2022**, *3*, 19. [[CrossRef](#)] [[PubMed](#)]
45. Manhas, K.R.; Blattman, J.N. Flow cytometry analysis of immune cell responses. *Methods Mol. Biol.* **2023**, *2597*, 105–120. [[PubMed](#)]

**Disclaimer/Publisher’s Note:** The statements, opinions and data contained in all publications are solely those of the individual author(s) and contributor(s) and not of MDPI and/or the editor(s). MDPI and/or the editor(s) disclaim responsibility for any injury to people or property resulting from any ideas, methods, instructions or products referred to in the content.